Supplement of Atmos. Chem. Phys., 23, 14813–14828, 2023
https://doi.org/10.5194/acp-23-14813-2023-supplement

Atmospheric Chemistry and Physics
Open Access

Supplement of

Photochemical ageing of aerosols contributes significantly to the production of atmospheric formic acid

Yifan Jiang et al.

Correspondence to: Tao Wang (tao.wang@polyu.edu.hk)

Table of contents

Text S1. Sampling of aerosol filters.

We collected ambient aerosols at Cape D'Aguilar Super Site in Autumn for photochemical aging experiments. The $PM_{2.5}$ samples were collected on quartz-fiber filters (8 × 10 inches) using a PUF-1000 high-volume sampler with a flow rate of 999 Lpm in 2020. All samplings were performed from 11:00 am local time (LT) to 10:00 am LT of the next day. The filters were pre-fired at 900 ℃ for 4 hours to remove organic artifacts and stored in a freezer at -20 ℃. Fractions with a given surface area from one randomized-chosen filter were used to perform the photochemical experiments or other analyses.

Text S2. The determination of $J_{NO_3^-(aq)}$ and $J_{O_3 \rightarrow O^1D}$ in the chamber and ambient air.

The $J_{NO_3^-(aq)}$ and $J_{O_3 \rightarrow O^1D}$ in the chamber was calculated by (Eq. (1)),

$$J = \int q(\lambda)\sigma(\lambda)I(\lambda)d\lambda \qquad (1)$$

where q(λ) is the quantum yield at wavelength λ (nm); σ(λ) is the cross-section at wavelength λ; I(λ) is the flux of xenon lamp at wavelength λ and was calculated by converting the irradiation energy spectra of the lamp (Fig. 4d) to photon flux based on Planck's equation. The q(λ) and σ(λ) of aqueous nitrate at 298 K were derived from (Chu and Anastasio, 2003). The q(λ) and σ(λ) of O_3 generating O^1D were adopted from the recommended value from IUPAC under 298 K (https://uv-vis-spectral-atlas-mainz.org/uvvis/index.html). The $J_{NO_3^-(aq)}$ and $J_{O_3 \rightarrow O^1D}$ in the ambient was calculated by the Tropospheric Ultraviolet and Visible (TUV) radiation model (https://www.acom.ucar.edu/Models/TUV/Interactive_TUV/) under clear sky conditions and then scaled to the field-measured jNO_2.

Text S3. Additional setting information on the box model simulation.

The data of trace gases (including O_3, NO, NO_2, CO and SO_2) and data obtained by ToF-CIMS (including HONO and N_2O_5) were averaged to one-hour resolution. For missing values of VOCs species, linear interpolations were applied. The missing J_{NO2} data was filled in using the data calculated by the Tropospheric Ultraviolet and Visible (TUV) Radiation Model (https://www2.acom.ucar.edu/modeling/tropospheric-ultraviolet-and-visible-tuv-radiation-model) and then scaled using measured J_{NO2}. Since the OVOCs data was not available during most of the modelling period, we run the model using measured VOCs concentration for three replicates to stabilise the intermediate species it generated and assumed the output concentrations of OVOCs were equal to the ambient values. We compared the simulated HCOOH concentration on 28 September where the ambient measured OVOCs data was available using modelled and measured values (Fig. S8). The uncertainty caused by using modelled OVOCs values is negligible. The methane concentration was assumed to remain

constant (2000 ppb; Peng et al., 2022), due to a lack of measurement data. The variable "ModelOptions.EndPointsOnly" was set to "1" because we only want the last point of each step. The "ModelOptions.LinkSteps" were set to "1" so that non-constrained species are carried over between steps. The variable "ModelOptions.IntTime" was set to "3600" meaning that the integration time for each step was 3600s. No family conservation was used. Readers are referred to a F0AM description paper for more information (Wolfe et al., 2016).

The biogenic emissions of HCOOH were calculated using the exponential temperature dependence algorithm of the Model of Emissions of Gases and Aerosols from Nature version 2.1 (MEGAN v2.1) (Guenther et al., 2012), as shown in (Eq. (2)).

$$E = \varepsilon \mathrm{LAI} \gamma_P \gamma_T \quad (2)$$

where E is the biogenic emission of HCOOH (μg m^{-2} h^{-1}); ε is the emission factor under standard environmental conditions (30 μg m^{-2} h^{-1}, Paulot et al. 2011); LAI is the leaf area index (3.65 m^2 m^{-2}, Myneni et al., 2021); γ_P and γ_T are the emission activity factors accounting for variability in light and temperature. In particular, γ_P was calculated using the PCEEA algorithm described by Guenther et al. (2006) and γ_T was calculated following Paulot et al. (2011).

Text S4. Additional laboratory experiments.

Since HONO and HCOOH were simultaneously observed during the photochemical aging process, it is possible that HCOOH was produced from the heterogeneous reactions between gas-phase OH radicals and particles. To check this possibility, an experiment was conducted as follows (Fig. S9). 4 Lpm HONO-containing air (78% RH, 7.2 ppb HONO, balanced with zero air) was injected into the chamber. The solution was prepared with 0.15 wt.% HCHO but without adding $NaNO_3$. The pH of the solution was also adjusted to 2.7 using sulfuric acid. The background HCOOH concentration was determined as 308.9 ppt when illuminating the chamber without the solution. After adding the solution, the HCOOH concentration increased to 428.8 ppt. After normalizing the HONO concentration in this experiment to that in the previous solution experiments containing $NaNO_3$ (0.77 ppb HONO, 0.62 ppb HCOOH) (Fig. 4c), the increased HCOOH concentration is 12.8 ppt, which is negligible. The conclusion is the same when compared with the filter irradiation experiments (4.1 ppb HONO, 5.6 ppb HCOOH). Therefore, the HONO photolysis contributes little to HCOOH production.

Text S5. Evaluation methods of HCOOH production from photochemical aging of aerosols using the Atmospheric Tomography Mission (ATom) data.

We first assessed the production of HCOOH from aerosols over the Pacific as an illustrative case of the remote marine boundary layer. The selected observation data

were obtained within the Pacific Ocean with sampling heights below 5 km. The mean values of mass concentration of PM_1, the surface area density of PM_1, the photolysis frequency of NO_2 and the mixing ratio of O_3 were 1 μg cm^{-3}, 26 μm^2 cm^{-3}, 0.01 s^{-1} and 24.2 ppb, respectively. The calculated mean production rate of HCOOH from aerosols ($P_{HCOOH\text{-}a}$) was 6.6 ppt h^{-1}. Considering that the proportion of nitrate in PM_1 was only 3%, which is significantly lower than that at our site (24.3%), the actual $P_{HCOOH\text{-}a}$ is expected to be even lower. The small $P_{HCOOH\text{-}a}$ in the remote marine atmosphere is reasonable given the low concentration of HCOOH observed over the Pacific (mean: 10.5 ppt; maximum: 85.6 ppt). In addition, a previous study showed small discrepancy between observed and modeled results in remote clean air masses in remote clean air masses (Chen et al., 2021).

We also assessed the HCOOH production when the remote marine boundary layer is affected by fire plumes by selecting data obtained at heights below 5 km and HCOOH concentrations higher than 1 ppb. The mean values of the mass concentration of PM_1, the surface area density of PM_1, the photolysis frequency of NO_2 and the mixing ratio of O_3 were 4.9 μg cm^{-3}, 92.6 μm^2 cm^{-3}, 0.011 s^{-1} and 45.5 ppb, respectively. The resulting $P_{HCOOH\text{-}a}$ was 84.5 ppt h^{-1}, significantly higher than that observed in remote marine atmosphere. After consideration of the low proportion of nitrate in PM_1 (5.1%), $P_{HCOOH\text{-}a}$ was 17.7 ppt h^{-1} assuming a positive linear correlation between $P_{HCOOH\text{-}a}$ and nitrate concentration. This corresponds to a rate of 2390%/year that organic aerosol (OA) mass (3 μg cm^{-3}) is photochemically converted to HCOOH, which is equivalent to a carbon-based HCOOH yield of~3.8−38% over 1−10 days of aging, close to that required to account for the ATom observations (16−37%) in aged fire air masses (Chen et al., 2021).

Supplementary figures

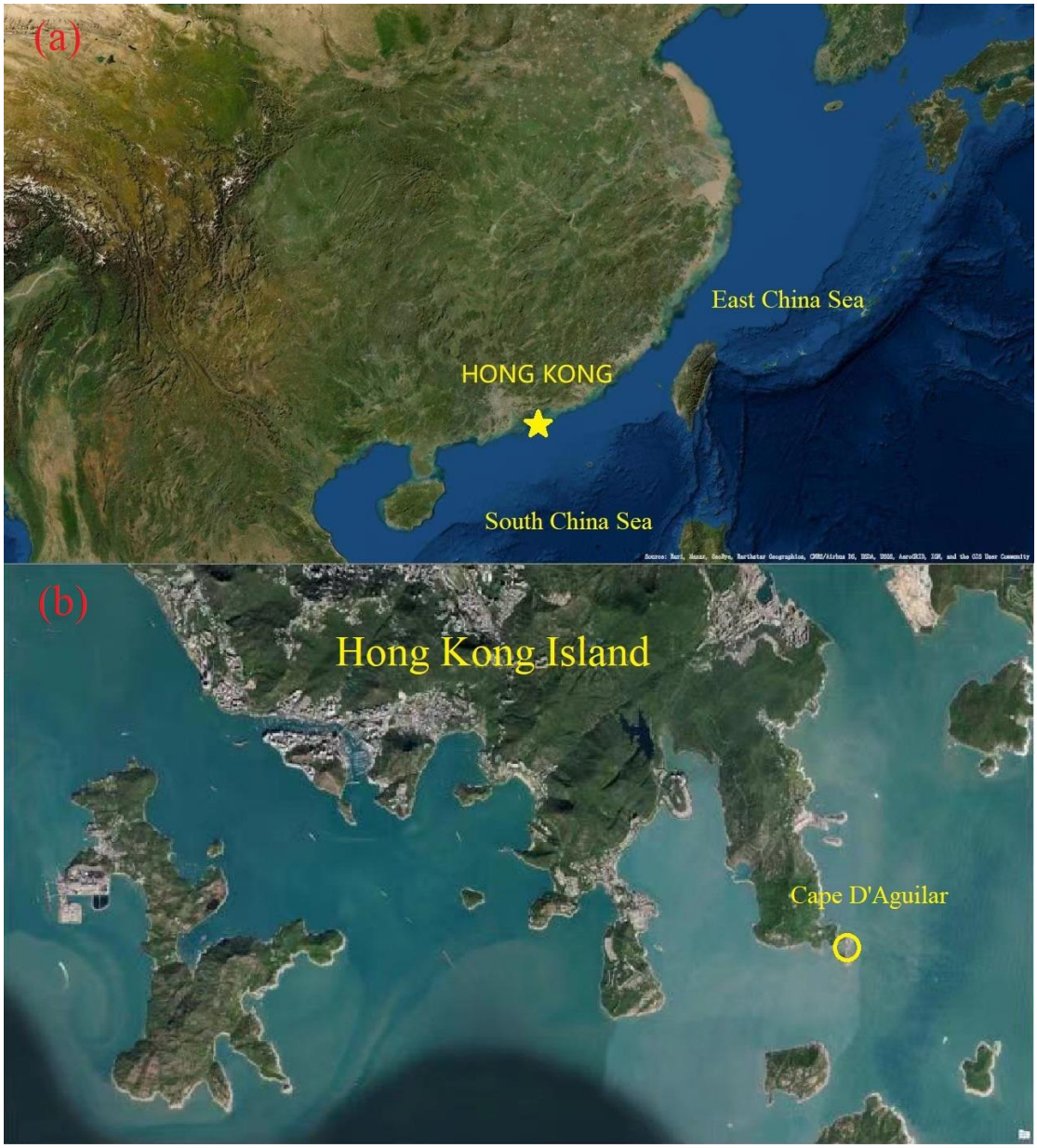

Figure S1. The location of the observation site, Cape D'Aguilar. (a) The location of Hong Kong in South China. (b) The field observation site in Hong Kong Island. The source is from Esri, Maxar, GeoEye, Earthstar Geographics, CNES/Airbus DS, USDA, USGS, AeroGRID, IGN, and the GIS User Community.

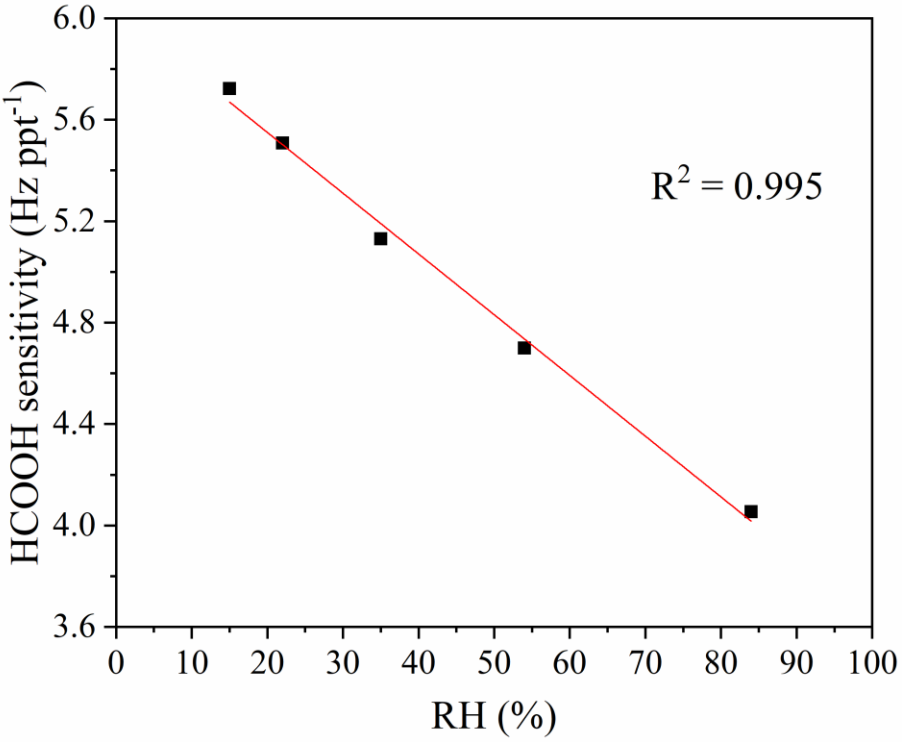

Figure S2. The variation of HCOOH sensitivity with RH.

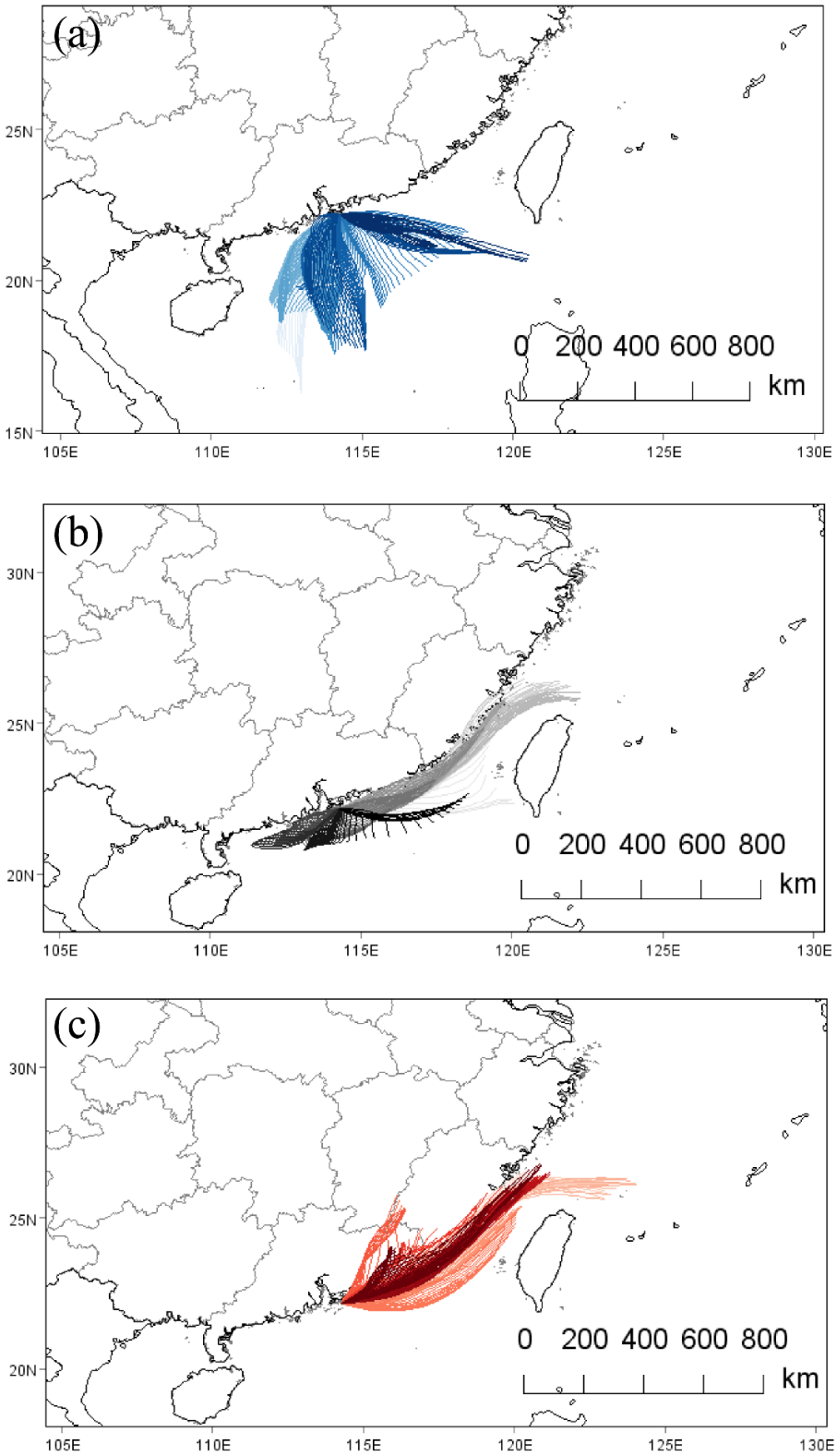

Figure S3. The backward trajectories of different kinds of air masses during the field campaign including 24-h backward trajectories of (a) the marine air masses occurred during 16–26 August and 11–23 September except 12, 15, and 16 September, (b) the haze period occurred from 24 September to 2 October and (c) the coastal air masses occurred during 4–31 October. The colour of the line deepens over time.

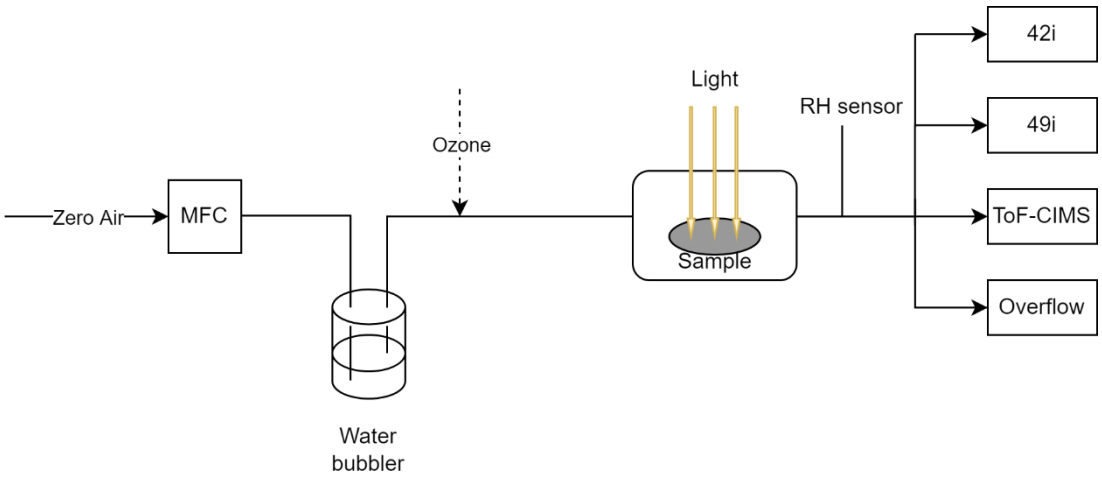

Figure S4. The schematic diagram of the photochemical aging experiment.

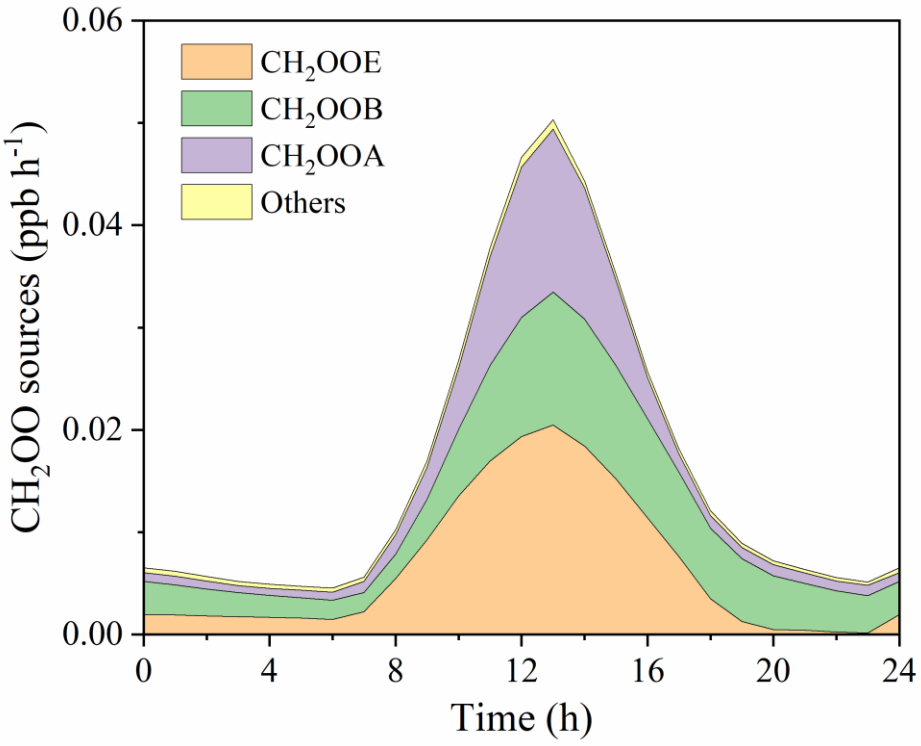

Figure S5. The sources of CH_2OO in the modified case on averaged diurnal profile during the whole campaign.

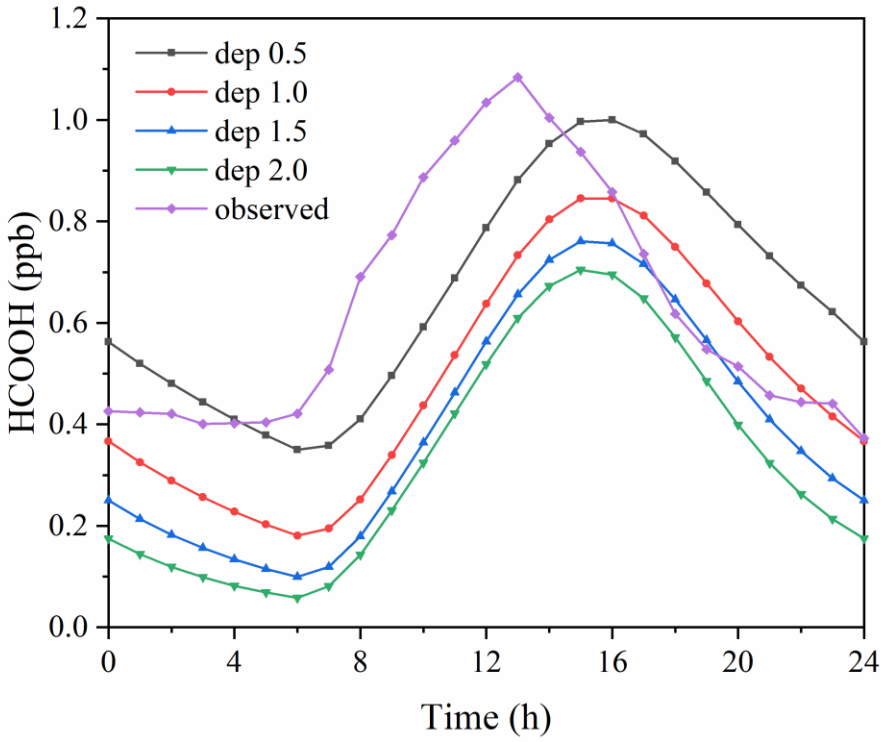

Figure S6. The sensitivity test of deposition velocity on averaged diurnal profile during the whole campaign in Scenario 4.

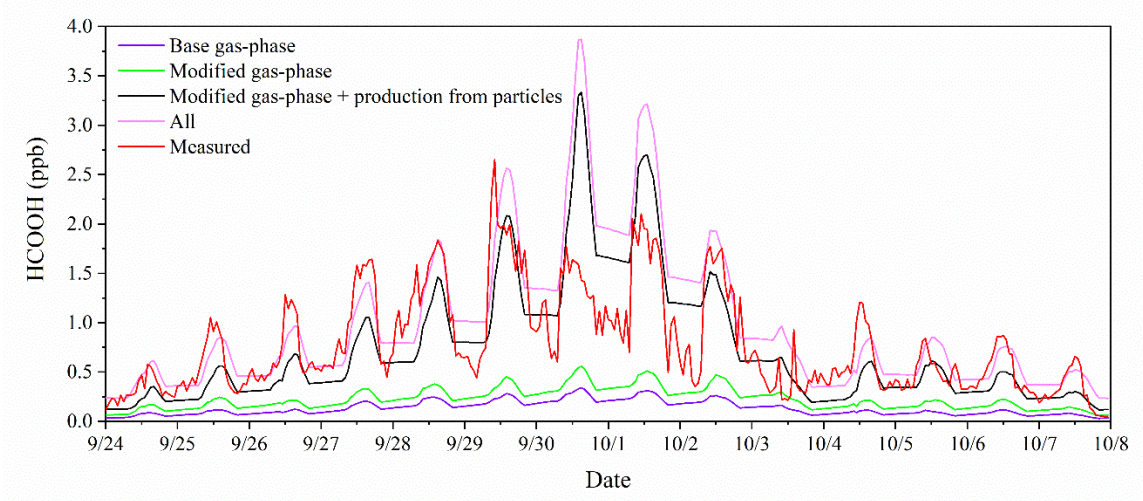

Figure S7. The model results of the simulation of two weeks using bimodal physical loss rates.

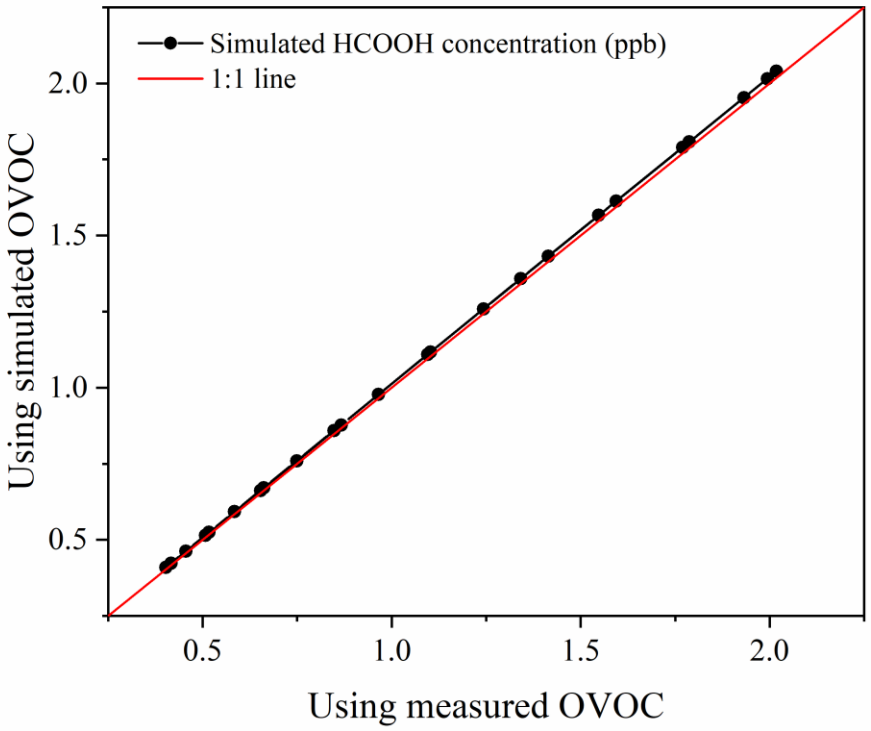

Figure S8. Comparison of simulated HCOOH concentration on 28 September using measured and simulated OVOCs values.

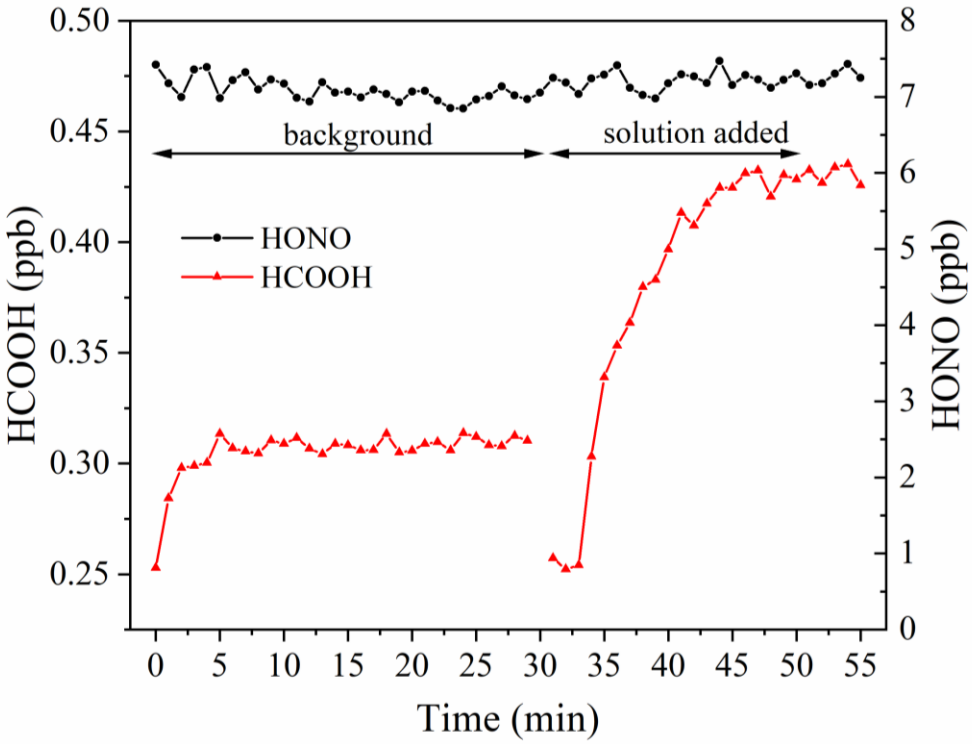

Figure S9. Additional laboratory experiments show that HCOOH was produced by nitrate rather than HONO.

Supplementary tables

Table S1. The instruments and measured species or parameters in the field campaign.

Species	Instruments	Time resolution
HCOOH, HONO, N_2O_5	Iodide-ToF-CIMS, Aerodyne Inc.	1 s
O_3	O_3 analyzer, model 49i, Thermo Scientific	1 min
NO, NO_2	NO_x analyzer, model 42i-TL with photolytic converter, Thermo Scientific	1 min
CO	CO analyzer, model T300U, Teledyne	1 min
SO_2	SO_2 analyzer, model T100U, Teledyne	1 min
jNO_2	Filter Radiometer, Metcon	1 min
VOCs	GC-MS/FID, Chromatotec Group	1 h
OVOCs	Carbonyl sampler, model 8000-2, ATEC HPLC	3 h
Particle number size distribution	Scanning mobility particle sizer, TSI	5 min
Compositions in $PM_{2.5}$ and PM_{10} (including Na^+, NH_4^+, K^+, Mg^{2+}, Ca^{2+}, Cl^-, NO_3^-, SO_4^{2-}	MARGA	1 h

Table S2. Summary of the $PM_{2.5}$ sampling information.

Date	RH	Size (cm^2)	Aerosol loading (mg)	Dry-state Surface area density
2020.10.07	72.34	51.6	3.33	192.52
2020.10.08	68.39	53.4	3.55	195.89
2020.10.26	78.85	53.4	4.28	119.86
2020.11.02	65.68	56.1	5.55	251.79

2020.11.03	69.82	52.51	4.40	233.81
2020.11.04	58.30	55.35	2.77	170.15
2020.11.05	76.32	53.352	1.95	134.89

Reference

Chu, L. and Anastasio, C.: Quantum Yields of Hydroxyl Radical and Nitrogen Dioxide from the Photolysis of Nitrate on Ice, Journal of Physical Chemistry A, 107, 9594–9602, https://doi.org/10.1021/jp0349132, 2003.

Guenther, A., Karl, T., Harley, P., Wiedinmyer, C., Palmer, P. I., and Geron, C.: Atmospheric Chemistry and Physics Estimates of global terrestrial isoprene emissions using MEGAN (Model of Emissions of Gases and Aerosols from Nature), Atmos. Chem. Phys, 6, 3181–3210, 2006.

Guenther, A. B., Jiang, X., Heald, C. L., Sakulyanontvittaya, T., Duhl, T., Emmons, L. K., and Wang, X.: The Model of Emissions of Gases and Aerosols from Nature version 2.1 (MEGAN2.1): an extended and updated framework for modeling biogenic emissions, Geosci. Model Dev, 5, 1471–1492, https://doi.org/10.5194/gmd-5-1471-2012, 2012.

Paulot, F., Wunch, D., Crounse, J. D., Toon, G. C., Millet, D. B., Decarlo, P. F., Vigouroux, C., Deutscher, N. M., Abad, G. G., Notholt, J., Warneke, T., Hannigan, J. W., Warneke, C., De Gouw, J. A., Dunlea, E. J., De Mazière, M., Griffith, D. W. T., Bernath, P., Jimenez, J. L., and Wennberg, P. O.: Importance of secondary sources in the atmospheric budgets of formic and acetic acids, Atmos Chem Phys, 11, 1989–2013, https://doi.org/10.5194/acp-11-1989-2011, 2011.

Peng, X., Wang, T., Wang, W., Ravishankara, A. R., George, C., Xia, M., Cai, M., Li, Q., Salvador, C. M., Lau, C., Lyu, X., Poon, C. N., Mellouki, A., Mu, Y., Hallquist, M., Saiz-Lopez, A., Guo, H., Herrmann, H., Yu, C., Dai, J., Wang, Y., Wang, X., Yu, A., Leung, K., Lee, S., and Chen, J.: Photodissociation of particulate nitrate as a source of daytime tropospheric Cl2, Nat Commun, 13, https://doi.org/10.1038/s41467-022-28383-9, 2022.

Wolfe, G. M., Marvin, M. R., Roberts, S. J., Travis, K. R., and Liao, J.: The framework for 0-D atmospheric modeling (F0AM) v3.1, Geosci Model Dev, 9, 3309–3319, https://doi.org/10.5194/GMD-9-3309-2016, 2016.